Multifunctional ZrB_2-rich $Zr_{1-x}Cr_xB_y$ thin films with enhanced mechanical, oxidation, and corrosion properties

Bakhit, Babak; Dorri, Samira; Kooijman, Agnieszka; Wu, Zhengtao; Lu, Jun; Rosen, Johanna; Mol, Johannes M.C.; Hultman, Lars; Petrov, Ivan; Greene, J. E.

DOI
10.1016/j.vacuum.2020.109990

Publication date
2021

Document Version
Final published version

Published in
Vacuum

Vacuum 185 (2021) 109990

Contents lists available at ScienceDirect

Vacuum

journal homepage: http://www.elsevier.com/locate/vacuum

Multifunctional ZrB_2-rich $Zr_{1-x}Cr_xB_y$ thin films with enhanced mechanical, oxidation, and corrosion properties

Babak Bakhit [a,*], Samira Dorri [a], Agnieszka Kooijman [b], Zhengtao Wu [c], Jun Lu [a], Johanna Rosen [a], Johannes M.C. Mol [b], Lars Hultman [a], Ivan Petrov [a,d,e], J.E. Greene [a,d,e], Grzegorz Greczynski [a]

[a] Thin Film Physics Division, Department of Physics (IFM), Linköping University, Linköping SE, 58183, Sweden
[b] Department of Materials Science and Engineering, Delft University of Technology, Delft, 2628CD, the Netherlands
[c] School of Electromechanical Engineering, Guangdong University of Technology, Guangzhou, 510006, China
[d] Materials Research Laboratory and Department of Materials Science, University of Illinois, Urbana, IL, 61801, USA
[e] Department of Materials Science and Engineering, National Taiwan University of Science and Technology, Taipei, 10607, Taiwan

ARTICLE INFO

Keywords:
Thin films
Transition-metal (TM) diborides
Mechanical properties
Wear
Oxidation
Corrosion

ABSTRACT

Refractory transition-metal (TM) diborides have high melting points, excellent hardness, and good chemical stability. However, these properties are not sufficient for applications involving extreme environments that require high mechanical strength as well as oxidation and corrosion resistance. Here, we study the effect of Cr addition on the properties of ZrB_2-rich $Zr_{1-x}Cr_xB_y$ thin films grown by hybrid high-power impulse and dc magnetron co-sputtering (Cr-HiPIMS/ZrB_2-DCMS) with a 100-V Cr-metal-ion synchronized bias. Cr metal fraction, $x = Cr/(Zr + Cr)$, is increased from 0.23 to 0.44 by decreasing the power P_{ZrB_2} applied to the DCMS ZrB_2 target from 4000 to 2000 W, while the average power, pulse width, and frequency applied to the HiPIMS Cr target are maintained constant. In addition, y decreases from 2.18 to 1.11 as a function of P_{ZrB_2}, as a result of supplying Cr to the growing film and preferential B resputtering caused by the pulsed Cr-ion flux. $ZrB_{2.18}$, $Zr_{0.77}Cr_{0.23}B_{1.52}$, $Zr_{0.71}Cr_{0.29}B_{1.42}$, and $Zr_{0.68}Cr_{0.32}B_{1.38}$ films have hexagonal AlB_2 crystal structure with a columnar nanostructure, while $Zr_{0.64}Cr_{0.36}B_{1.30}$ and $Zr_{0.56}Cr_{0.44}B_{1.11}$ are amorphous. All films show hardness above 30 GPa. $Zr_{0.56}Cr_{0.44}B_{1.11}$ alloys exhibit much better toughness, wear, oxidation, and corrosion resistance than $ZrB_{2.18}$. This combination of properties makes $Zr_{0.56}Cr_{0.44}B_{1.11}$ ideal candidates for numerous strategic applications.

1. Introduction

Transition-metal (TM) nitride coatings have many industrial applications from mechanical components in aerospace industry to cutting tools [1–4]. Metastable NaCl-structure $Ti_{1-x}Al_xN$ layers grown by magnetron sputtering are the most attractive group of TiN-based thin films, suitable as protective coatings for cutting tools, which show good hardness (typically ~30 GPa), high wear and oxidation resistance (depending on Al concentration), and self-hardening effects at elevated temperatures up to ~900 °C (resulting from spinodal decomposition) [3–5]. However, the ever-increasing demand from industry for enhanced coating properties motivates the search for alternatives.

One particularly promising group of materials are TM diborides, extensively studied in the recent years. TM diborides, which typically crystallize in a hexagonal AlB_2 structure (*P6/mmm*, SG-191) – where B atoms form graphite-like honeycomb sheets between hexagonal-close-packed TM layers [6,7], exhibit high melting points, excellent hardness, high thermal and chemical stability, and good conductivity [8]. This unique combination of properties originates from their dual ceramic/metallic nature where strong combined covalent/ionic bonding between TM and B atoms together with the covalent bonding within the honeycomb B sheets provide high melting point, hardness, and stiffness [9,10], while metallic bonding between TM atoms results in good thermal and electrical conductivities [6]. Hence, TM diborides are good candidates for a broad range of applications, particularly in extreme environments, such as hypersonic aerospace vehicles [11,12], rockets [12], nuclear reactors [8], optoelectronic and microelectronic components [13,14], solar power [15], and cutting tools [16–20].

* Corresponding author.
E-mail address: babak.bakhit@liu.se (B. Bakhit).

https://doi.org/10.1016/j.vacuum.2020.109990
Received 26 October 2020; Received in revised form 4 December 2020; Accepted 6 December 2020
Available online 8 December 2020

However, compared to TiAlN, the industrial applications of sputter-deposited TM diboride thin films are very limited, primarily due to poor oxidation resistance [16] and high brittleness [17]. Bulk diborides, which are mostly synthesized by powder metallurgy processes [11,21], start to oxidize at temperatures below ~450 °C with oxidation products that are typically TMO_2 and glassy B_2O_3 phases [22]. The B_2O_3 phase tends to rapidly evaporate at temperatures above ~1000 °C which results in the formation of a porous oxide scale that does not passivate the surface against oxidation [22]. This issue is even worse for the TM diboride thin films that are overstoichiometric (B/TM ratios > 2), in which oxide scales formed at temperatures above ~400 °C are highly B deficient with no oxidation protection; causing a poor oxidation resistance [16]. Similar to TiN-based thin films, alloying TM diborides with Al enhances their oxidation properties [16].

Moreover, the applications of sputter-deposited TM diborides are restricted due to their inherent brittleness [17]. Although these films have high hardness ranging from 30 to 50 GPa [20,23,24], this alone is not sufficient for preventing failure in applications which involve high mechanical stresses. Hardness is usually accompanied by brittleness that causes crack formation and propagation at the presence of high stresses [25]. Hence, TM diboride films require to have a combination of high hardness and ductility (referred to as toughness [26]) in order to avoid brittle cracking. To accommodate this requirement, we recently showed that alloying ZrB_2 thin films with Ta can result in a simultaneous increase in both nanoindentation hardness and toughness [17]. $Zr_{1-x}Ta_xB_y$ alloys with $x \geq 0.2$ exhibit a self-organized columnar core/shell nanostructure in which crystalline Zr-rich stoichiometric $Zr_{1-x}Ta_xB_2$ cores are surrounded by narrow dense, disordered Ta-rich (B-deficient) shells that have the structural characteristics of metallic-glass thin films; both high strength and toughness [18]. These layers also show a high thermal stability in which their hardness increases as a function of annealing temperature up to 800 °C. The age hardening observed in the $Zr_{1-x}Ta_xB_y$ films with $0 \leq x \leq 0.3$, which occurs without any phase separation or decomposition, can be explained by point-defect recovery that enhances the chemical bond density [20]. For temperatures above 800 °C, hardness decreases due to recrystallization, column coarsening, and stacking fault annihilation. All $Zr_{1-x}Ta_xB_y$ films generally have hardness values H > 34 GPa up to 1200 °C [20].

Here, we study the effect of Cr addition on the properties of ZrB_2-rich $Zr_{1-x}Cr_xB_y$ thin films grown by hybrid high-power impulse and dc magnetron co-sputtering (Cr-HiPIMS/ZrB_2-DCMS) as alloying with Cr previously showed enhanced oxidation [27,28], wear [29,30], and corrosion [30,31] properties for TM nitrides. The B/(Zr + Cr) ratio y decreases, while the Cr/(Zr + Cr) ratio x increases, gradually from $ZrB_{2.18}$ to $Zr_{0.77}Cr_{0.23}B_{1.52}$, $Zr_{0.71}Cr_{0.29}B_{1.42}$, $Zr_{0.68}Cr_{0.32}B_{1.38}$, $Zr_{0.64}Cr_{0.36}B_{1.30}$, and $Zr_{0.56}Cr_{0.44}B_{1.11}$ by decreasing the power P_{ZrB_2} applied to the DCMS ZrB_2 target from 4000 to 2000 W in 500-W increments, while other deposition parameters are maintained constant. All films have nanoindentation hardnesses H > 30 GPa. The toughness, wear, oxidation, and corrosion resistance of the films increase as a function of Cr concentration. Films with the highest Cr content, $Zr_{0.56}Cr_{0.44}B_{1.11}$, exhibit a combination of enhanced properties.

2. Experimental

$Zr_{1-x}Cr_xB_y$ thin films are grown in a CC800/9 CemeCon AG sputtering system equipped with rectangular 8.8 × 50 cm^2 stoichiometric ZrB_2 and elemental Cr targets. Al_2O_3(0001), Si(001), and WC-Co substrates, 1.5 × 1.5 cm^2, are cleaned sequentially in acetone and isopropyl alcohol, and then mounted symmetrically with respect to the targets, which are tilted toward the substrates resulting in a 21° angle between the substrate normal and the normal to each target. The target-to-substrate distance is 20 cm. The chamber is degassed before deposition by applying 8.8 kW to each of two resistive heaters for 2 h, which results in a temperature of ~475 °C at the substrate position. The system base pressure is 3.8×10^{-6} Torr (0.5 mPa). The film growth is carried out at ~475 °C and a total Ar pressure of 3 mTorr (0.4 Pa). Prior to deposition, the targets are sequentially DCMS sputter-cleaned in Ar at 2 kW for 60 s with shutters protecting the substrate table and the opposite target. A thin continuous Cr buffer layer, with a thickness of 4 ± 1 nm, is initially deposited on all substrates to improve adhesion and minimize their influence on the film morphological evolution.

ZrB_y films are grown by DCMS with a target power of 4 kW and a negative dc substrate bias of 100 V. For growing the $Zr_{1-x}Cr_xB_y$ films, a hybrid target-power scheme [32] (Cr-HiPIMS/ZrB_2-DCMS) is employed in which the ZrB_2 target is continuously sputtered by DCMS, while the Cr magnetron is operated in HiPIMS mode to provide pulsed Cr ion fluxes. The Cr metal fraction, Cr/(Zr + Cr), is increased from 0.23 to 0.44 by decreasing the power P_{ZrB_2} applied to the DCMS ZrB_2 target from 4000 to 2000 W in 500-W increments, while the average power, pulse width, and frequency applied to the HiPIMS Cr target are maintained constant at 700 W, 50 μs, and 100 Hz, respectively. This results in a constant peak Cr-target current density of ~0.73 A/cm^2. A negative substrate bias of 100 V is applied in synchronous with the 100-μs metal-ion-rich portion of each HiPIMS pulse, starting 30 μs after the cathode HiPIMS pulse. The substrates are at a negative floating potential of 10 V at all other times. The film deposition rate is ~0.85 nm/s for $ZrB_{2.4}$, while it increases from ~0.45 nm/s for P_{ZrB_2} = 2000 W to ~0.78 nm/s for P_{ZrB_2} = 4000 W for the $Zr_{1-x}Cr_xB_y$ films.

Cross-sectional scanning electron microscopy (XSEM) analyses are conducted in a Zeiss LEO 1550 electron microscope to obtain the thicknesses and cross-sectional morphologies of the films. θ-2θ X-ray diffraction (XRD) scans are carried out using a Philips X'Pert X-ray diffractometer with a Cu K_α source (λ = 0.15406 nm) to determine crystal structure and orientations of the layers. Film compositions are obtained from time-of-flight elastic recoil detection analyses (ToF-ERDA) in a tandem accelerator with a 36 MeV $^{127}I^{8+}$ probe beam incident at 67.5° with respect to the sample surface normal. Recoils are detected at 45°. Chemical bonding in the films is evaluated by X-ray photoelectron spectroscopy (XPS) using a Kratos Axis Ultra DLD instrument employing monochromatic Al K_α radiation (hν = 1486.6 eV). All surfaces are sputter-etched for 120 s with a 4-keV Ar^+ ion beam incident at 70° with respect to the sample normal. Then, the Ar^+ ion energy is reduced to 0.5 keV for 600 s to minimize surface damage. The analyzed area, which is located in the center of a 3 × 3 mm^2 ion-etched region, is 0.3 × 0.7 mm^2. The core level spectra are referenced to the Fermi edge cut-off to avoid problems caused by the referencing method based on the C 1s peak from adventitious carbon [33].

Cross-sectional transmission electron microscopy (XTEM) analyses are carried out in a monochromated and double-corrected FEI Titan^3 60–300 electron microscope operated at 300 kV. Images are acquired using bright-field (BF) and dark-field (DF) TEM imaging modes. TEM specimens are prepared by mechanical polishing, followed by Ar^+ ion milling at 5 keV, with a 3° incidence angle, on both sides of each sample during rotation, in a Gatan precision ion miller. The specimens are finally sputter-cleaned using an ion energy of 0.5 keV without changing the angle of incident Ar^+ ions.

The in-plane residual stresses of $Zr_{1-x}Cr_xB_y$ thin films are obtained using the modified Stoney equation by determining the substrate wafer curvature from XRD rocking-curve measurements. More details are provided in reference 17. The nanoindentation analyses of the layers are performed in an Ultra-Micro Indentation System with a sharp Berkovich diamond tip calibrated using a fused-silica standard. For hardness H and elastic modulus E measurements, the layers are indented using a fixed load of 12 mN, while indention depths are maintained below 10% of the film thickness. Reported values are the average of 35 indentations. The results are analyzed using the Oliver and Pharr method [34]. The films are also indented by a diamond cube-corner tip with a load of 200 mN to measure the average lengths of induced radial cracks. The average crack length, which is an indication of nanoindentation toughness [35], is obtained from four cube-corner indents for each film.

To evaluate the films' adhesion and toughness, the Revescratch tests

are performed using an Anton-Paar-TriTec UNHT^3 system equipped with a Rockwell-C diamond indenter with a tip radius of 100 μm. A progressive loading regime is used in which the load is linearly increased from 1 to 80 N with a rate of 158 N/min. The scratch length is 3 mm with a speed of 6 mm/min. The same equipment with a ball-on-disc tribometer with a 3-mm-diameter GCR15 steel ball is also used to investigate the friction and wear properties of the layers at room temperature. A load of 2 N with 0.1 m/s sliding speed (2000 laps) is applied during the wear tests. The wear track profiles are measured by a confocal laser-scanning microscope. The wear rates are obtained using the following equation [36]:

2.1. Wear rate = $V/(F \times s)$

where V is the volume loss by wear (mm^3), F is the applied load (N), and s is the sliding distance (m).

$ZrB_{2.18}$ and $Zr_{0.56}Cr_{0.44}B_{1.11}$ thin films are annealed at 700 °C in air for times t_a ranging from 1.0 to 5.0 h using a high-temperature furnace from MTI Corporation (GSL-1100 × -S). The heating rate is constant at 10 °C/min, and the specimens are cooled down to room temperature, while the furnace is turned off.

Open circuit potential (E_{ocp}) with superimposed linear polarization resistance (R_p) followed by potentiodynamic polarization measurements are employed to study the corrosion resistance of $ZrB_{2.18}$ and $Zr_{0.56}Cr_{0.44}B_{1.11}$ thin films. All measurements are carried out in an aqueous 0.1 M NaCl corrosive medium, at room temperature and without agitation, using a Bio-logic VSP-300 potentiostat/galvanostat system. A standard three-electrode system is used with a silver/silver chloride electrode (Ag/AgCl) as the reference electrode, a platinum mesh as the counter electrode, and the films as the working electrode. The E_{ocp} values of the films immersed in the corrosive medium are monitored for 25 h and reported versus the Ag/AgCl reference electrode potential, unless mentioned differently. The R_p measurement is performed after 0.25, 0.5, 1.0, 2.0, 4.0, 8.0, 16.0, and 24.0 h of immersion by a sweeping potential of ±10 mV versus E_{ocp} with a scanning rate of 0.167 mV/s. The R_p values are obtained from the inverse of the slopes of current-potential plots at the corrosion potential (E_{corr}). Immediately afterward, the potentiodynamic polarization is performed with a sweeping rate of 0.167 mV/s from −160 to +1260 mV with respect to E_{ocp}. The corrosion potentials (E_{corr}) and current densities (i_{corr}) are calculated according to the Tafel extrapolation [37,38].

3. Results and discussion

3.1. Elemental compositions and microstructure

Table 1 gives the elemental compositions of as-deposited $Zr_{1-x}Cr_xB_y$ thin films obtained from ToF-ERDA measurements. The as-deposited ZrB_y films grown using DCMS at P_{ZrB_2} = 4000 W are over-stoichiometric with the B/(Zr + Cr) ratio y of 2.18. The Cr/(Zr + Cr) ratio, x, in the alloys deposited by hybrid Cr-HiPIMS/ZrB_2-DCMS co-sputtering increases from 0.23 for P_{ZrB_2} = 4000 W, to 0.29 for P_{ZrB_2} = 3500 W, 0.32 for P_{ZrB_2} = 3000 W, 0.36 for P_{ZrB_2} = 2500 W, and 0.44 for P_{ZrB_2} = 2000 W, while the B/(Zr + Cr) ratio, y, gradually decreases from 1.52 to 1.42, 1.38, 1.30, and 1.11 with decreasing P_{ZrB_2}. The total concentration of carbon, nitrogen, and oxygen is ≤ 1.6 at. %, and the Ar concentration is ≤ 0.5 at. % in all films. Alloying ZrB_y with Cr using a flux of energetic Cr ions bombarding the growing film not only adds Cr atoms, but it also affects the B content via preferential resputtering.

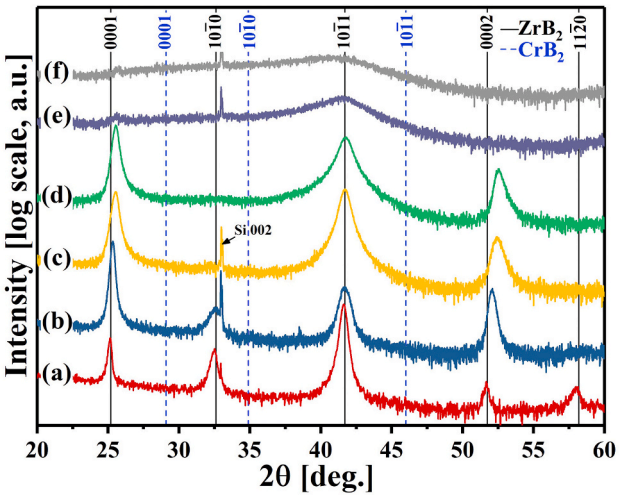

Fig. 1. XRD θ-2θ scans of as-deposited (a) $ZrB_{2.18}$, (b) $Zr_{0.77}Cr_{0.23}B_{1.52}$, (c) $Zr_{0.71}Cr_{0.29}B_{1.42}$, (d) $Zr_{0.68}Cr_{0.32}B_{1.38}$, (e) $Zr_{0.64}Cr_{0.36}B_{1.30}$, and (f) $Zr_{0.56}Cr_{0.44}B_{1.11}$ thin films grown on Si(001) substrates. The peak at 32.8° is the 002 forbidden reflection arising from Si(001) substrate, which appears due to multiple scattering events [42].

XRD θ-2θ scans of as-deposited $Zr_{1-x}Cr_xB_y$ thin films grown on Si (001) substrates are shown in Fig. 1. Vertical solid and dashed lines correspond to reference powder-diffraction peak positions for ZrB_2 [39] and CrB_2 [40], respectively. All reflections in the XRD patterns of $ZrB_{2.18}$, $Zr_{0.77}Cr_{0.23}B_{1.52}$, $Zr_{0.71}Cr_{0.29}B_{1.42}$, and $Zr_{0.68}Cr_{0.32}B_{1.38}$ films originate from the crystalline hexagonal AlB_2-type structure (solid-solution), while the patterns of $Zr_{0.64}Cr_{0.36}B_{1.30}$ and $Zr_{0.56}Cr_{0.44}B_{1.11}$ films show very low intensity (notice the logarithmic scale), broad 0001 and 10$\bar{1}$0 X-ray reflections; indicating that they are X-ray amorphous. The (10$\bar{1}$0) reflection disappears for $Zr_{0.71}Cr_{0.29}B_{1.42}$ and $Zr_{0.68}Cr_{0.32}B_{1.38}$ alloys. The formation of X-ray amorphous $Zr_{0.64}Cr_{0.36}B_{1.30}$ and $Zr_{0.56}Cr_{0.44}B_{1.11}$ films can be attributed to the collapse of the hexagonal AlB_2-structure that results from the lack of B between the hexagonal-close-packed $Zr_{1-x}Cr_x$ layers (y ≤ 1.30) as well as the difference between the crystal structures of Zr and Cr (Zr has a hexagonal close-packed structure, while Cr has a body-centered-cubic structure [41]).

While the position of (10$\bar{1}$1) reflections does not change with increasing the Cr concentration, the positions of (0001) and (0002) reflections shift toward higher 2θ values, corresponding to a decrease in the out-of-plane c lattice parameter from 0.352 nm for $ZrB_{2.18}$ to 0.349 nm for $Zr_{0.68}Cr_{0.32}B_{1.38}$. This is mainly due to the smaller covalent radius of Cr atoms incorporated in the diboride structure, the corresponding lower B concentrations, and a change in the film's residual stress level. The incorporation of Cr atoms also results in a significant increase in the

Table 1
Concentrations of primary elements, B, Cr, and Zr in as-deposited $Zr_{1-x}Cr_xB_y$ thin films grown on Si(001) substrates, obtained from ToF-ERDA, as a function of ZrB_2 target power P_{ZrB_2}. The total concentration of contaminants (not included in the table) is ≤ 2.1 at. %.

Films	P_{ZrB_2} [W]	B [at. %]	Cr [at. %]	Zr [at. %]	Cr/(Zr + Cr)	B/(Zr + Cr)
$ZrB_{2.18}$	4000	67.3 ± 1.0	0	30.9 ± 0.4	0	2.18
$Zr_{0.77}Cr_{0.23}B_{1.52}$	4000	59.6 ± 1.1	9.1 ± 0.3	30.0 ± 0.5	0.23	1.52
$Zr_{0.71}Cr_{0.29}B_{1.42}$	3500	57.6 ± 0.7	11.8 ± 0.2	28.9 ± 0.3	0.29	1.42
$Zr_{0.68}Cr_{0.32}B_{1.38}$	3000	57.2 ± 1.0	13.3 ± 0.1	28.1 ± 0.1	0.32	1.38
$Zr_{0.64}Cr_{0.36}B_{1.30}$	2500	55.4 ± 1.0	15.5 ± 0.4	27.2 ± 0.4	0.36	1.30
$Zr_{0.56}Cr_{0.44}B_{1.11}$	2000	51.6 ± 0.8	20.4 ± 0.4	25.9 ± 0.4	0.44	1.11

full-width at half-maximum values of the XRD reflections; e.g. from 0.18° for $ZrB_{2.18}$ to 0.4° for $Zr_{0.68}Cr_{0.32}B_{1.38}$ for the (0001) reflection.

B 1s, Zr 3d, and Cr 2p XPS core-level spectra acquired from the as-deposited $Zr_{1-x}Cr_xB_y$ thin films grown on Si(001) substrates are plotted in Fig. 2. The B 1s and Zr 3d spectra shown in Fig. 2(a) are normalized to the intensity of the Zr $3d_{5/2}$ peaks. The Zr $3d_{3/2}$ and $3d_{5/2}$ peaks appear at 181.3 and 178.9 eV, respectively, with no detectable change in their positions or shapes as a function of Cr concentration. The position of the B 1s peaks does not change noticeably for $ZrB_{2.18}$, $Zr_{0.77}Cr_{0.23}B_{1.52}$, $Zr_{0.71}Cr_{0.29}B_{1.42}$, and $Zr_{0.68}Cr_{0.32}B_{1.38}$; the peaks appear at ~188.0 eV. This indicates that the incorporation of Cr, which has a slightly higher electronegativity than Zr (1.66 for Cr and 1.33 for Zr, based on the Pauling scale [43]), does not change the effective valence-charge density residing on the B atoms. However, there is a slight shift in the position of the B 1s peaks toward lower binding energies for the $Zr_{0.64}Cr_{0.36}B_{1.30}$ and $Zr_{0.56}Cr_{0.44}B_{1.11}$ alloys (~187.7 eV). In addition, the width of B 1s peaks for these alloys is larger than the other films. These slight changes correlate to the apparent loss of crystalline structure (see Fig. 1) and, hence, cannot be directly related to the change in the bonding configuration, as likely the layer electrical properties are modified, which may have a direct effect on the screening ability [44]. Fig. 2(b) shows that increasing Cr concentration does not have an obvious effect on the positions and shapes of the Cr 2p peaks (the Cr 2p spectra in Fig. 2(b) are normalized to the intensity of the Cr $2p_{3/2}$ peaks).

Fig. 3 compares the XSEM, BF-XTEM, and DF-XTEM images of as-deposited $ZrB_{2.18}$, $Zr_{0.77}Cr_{0.23}B_{1.52}$, $Zr_{0.68}Cr_{0.32}B_{1.38}$, and $Zr_{0.56}Cr_{0.44}B_{1.11}$ thin films grown on Si(001) substrates. The corresponding selected-area electron diffraction (SAED) patterns are also shown as insets. The XTEM images and SAED patterns are acquired from regions close to the surface of the layers. The XSEM images, Figs. 3 (a)-3(d), show that all as-deposited films have dense microstructures with smooth surfaces. The $ZrB_{2.18}$ and $Zr_{0.77}Cr_{0.23}B_{1.52}$ films exhibit a columnar microstructure with columns extending through the films, while the XSEM images of $Zr_{0.68}Cr_{0.32}B_{1.38}$ and $Zr_{0.56}Cr_{0.44}B_{1.11}$ alloys are featureless. The BF- and DF-XTEM images of as-deposited $ZrB_{2.18}$ films, shown in Figs. 3(e) and 3(i), indicate that $ZrB_{2.18}$ consists of discernable porosities, marked by black arrows in the micrograph. The $ZrB_{2.18}$ columns with a width of 10.1 ± 2 nm near the film's surface are continual from close to the substrate toward the surface. The columns are inclined at an angle of 7° with respect to the substrate normal, due to the 21° angle between the substrate and the ZrB_2 target. The corresponding SAED pattern, the inset in Fig. 3(e), is composed of diffraction arcs with (0001), $(10\bar{1}0)$, and $(10\bar{1}1)$ components in which the (0001) signal in the growth direction is the weakest one, in agreement with the XRD result in Fig. 1(a).

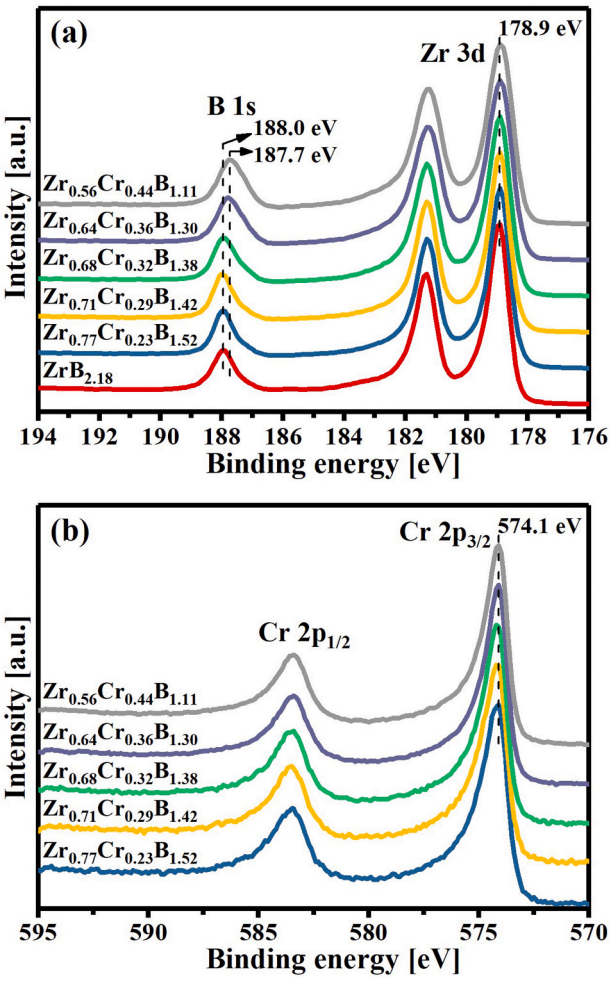

Fig. 2. (a) B 1s and Zr 3d and (b) Cr 2p XPS core-level spectra acquired from as-deposited $Zr_{1-x}Cr_xB_y$ thin films grown on Si(001) substrates.

The BF- and DF-XTEM images of $Zr_{0.77}Cr_{0.23}B_{1.52}$ and $Zr_{0.68}Cr_{0.32}B_{1.38}$, Figs. 3(f), (j), 3(g), and 3(k), show that alloying with Cr interrupts the continuous columnar growth and produces dense nanostructure. The column length of $Zr_{1-x}Cr_xB_y$ alloys decreases as a function of Cr concentration up to x = 0.32. Moreover, adding Cr leads to a decrease in the column width; the nanostructure of $Zr_{0.68}Cr_{0.32}B_{1.38}$ consists of very fine columns that do not extend throughout the whole film, see Figs. 3(g) and 3(k). The corresponding SAED patterns of $Zr_{0.77}Cr_{0.23}B_{1.52}$ and $Zr_{0.68}Cr_{0.32}B_{1.38}$ alloys, the insets in Fig. 3(f) and 3 (g), indicate the presence of (0001), $(10\bar{1}0)$, and $(10\bar{1}1)$ diffraction arcs with a decrease in the crystallinity by increasing the Cr concentration. The BF- and DF-XTEM micrographs of $Zr_{0.56}Cr_{0.44}B_{1.11}$ in Figs. 3(h) and 3(l), together with its corresponding high-resolution BF-XTEM image and SAED pattern shown as insets in Fig. 3(h), confirm that this alloy has an amorphous nanostructure, which is consistent with its XRD θ-2θ result in Fig. 1(f).

3.2. Mechanical properties

The residual stress of as-deposited $Zr_{1-x}Cr_xB_y$ thin films grown on Al_2O_3(0001) substrates changes from +0.91 ± 0.04 GPa for $ZrB_{2.18}$, to −0.83 ± 0.23 GPa for $Zr_{0.77}Cr_{0.23}B_{1.52}$, −1.27 ± 0.15 GPa for $Zr_{0.71}Cr_{0.29}B_{1.42}$, +0.15 ± 0.02 GPa for $Zr_{0.68}Cr_{0.32}B_{1.38}$, +0.04 ± 0.04 GPa for $Zr_{0.64}Cr_{0.36}B_{1.30}$, and −0.53 ± 0.02 GPa for $Zr_{0.56}Cr_{0.44}B_{1.11}$.

Fig. 4 shows the nanoindentation hardnesses H and elastic moduli E of as-deposited layers grown on Al_2O_3(0001) substrates as a function of x. The hardness of $ZrB_{2.18}$ is 31.8 ± 1.0 GPa, and increases to 41.7 ± 1.2 GPa for $Zr_{0.77}Cr_{0.23}B_{1.52}$ and 41.6 ± 0.9 GPa for $Zr_{0.71}Cr_{0.29}B_{1.42}$, which is primarily due to their high compressive stress, solid-solution hardening [45], and narrow column widths (Hall-Petch effect [46,47]). Further increase in Cr concentration results in a decrease in H to ~31.0 GPa for $Zr_{0.68}Cr_{0.32}B_{1.38}$, $Zr_{0.64}Cr_{0.36}B_{1.30}$, and $Zr_{0.56}Cr_{0.44}B_{1.11}$. The decrease in H can be attributed to their (i) low B concentration, which results in a decrease in the strong bond density, (ii) tensile residual stress, (iii) high Cr concentration, which shows similar effect on the hardness of TMCrN films [48,49], and (iv) structural change from crystalline to nanocrystalline to amorphous. The elastic modulus of $ZrB_{2.18}$ is 494 ± 19 GPa. E decreases from 507 ± 15 GPa for $Zr_{0.77}Cr_{0.23}B_{1.52}$, to 497 ± 11 GPa for $Zr_{0.71}Cr_{0.29}B_{1.42}$, 422 ± 19 GPa for $Zr_{0.68}Cr_{0.32}B_{1.38}$, and 404 ± 10 GPa for $Zr_{0.64}Cr_{0.36}B_{1.30}$. Then, it shows a slight increase to 408 ± 14 GPa for $Zr_{0.56}Cr_{0.44}B_{1.11}$.

The relative ductility of as-deposited $ZrB_{2.18}$, $Zr_{0.77}Cr_{0.23}B_{1.52}$, $Zr_{0.68}Cr_{0.32}B_{1.38}$, and $Zr_{0.56}Cr_{0.44}B_{1.11}$ thin films grown on Al_2O_3(0001) substrates is assessed by nanoindentation using a sharp cube-corner indenter. The minimum indentation force required to create radial cracks at nanoindentation corners is below 50 mN for $ZrB_{2.18}$, $Zr_{0.77}Cr_{0.23}B_{1.52}$, and $Zr_{0.68}Cr_{0.32}B_{1.38}$, while this force is 150 mN for the

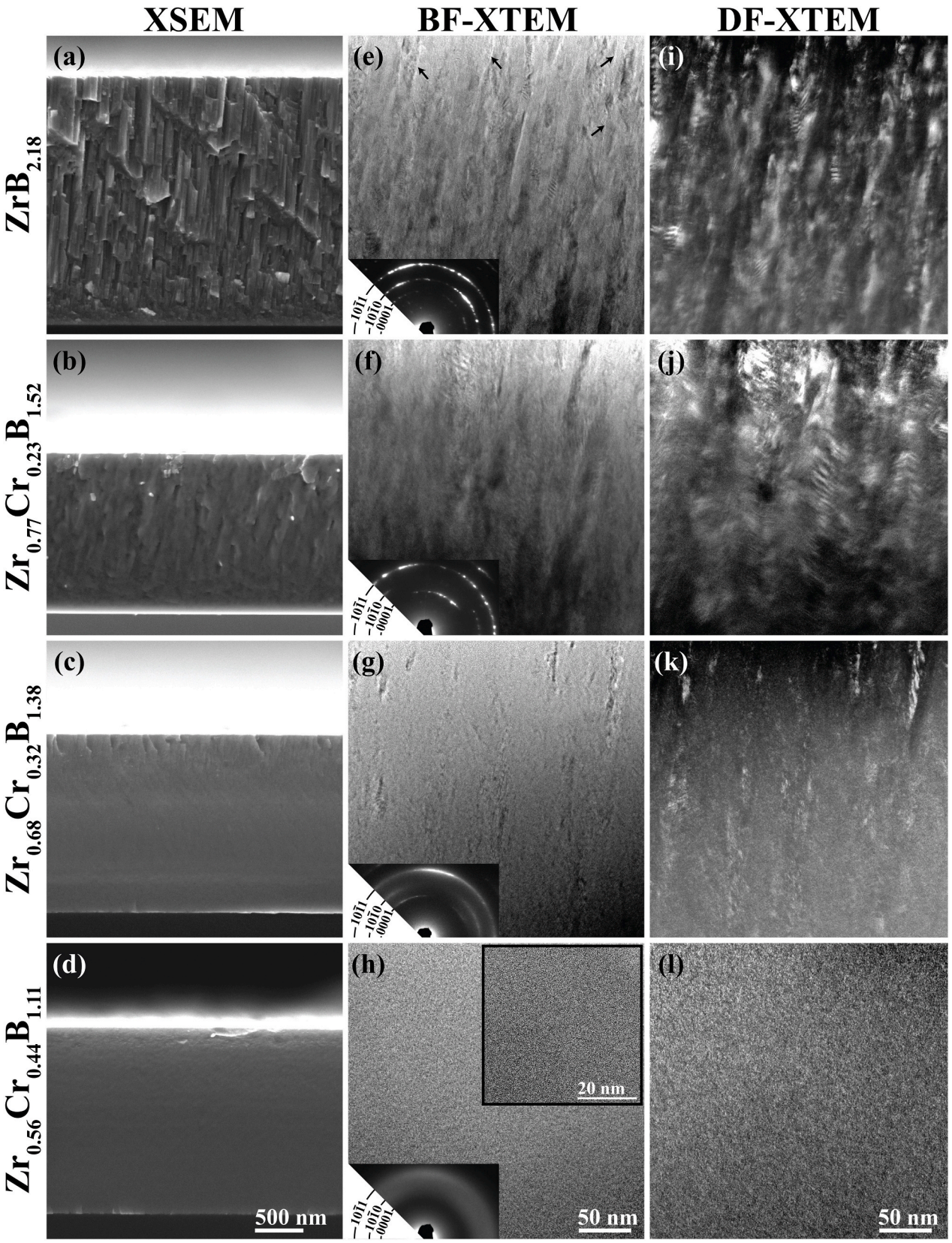

Fig. 3. XSEM, BF-XTEM, and DF-XTEM images of as-deposited (a, e, i) $ZrB_{2.18}$, (b, f, j) $Zr_{0.77}Cr_{0.23}B_{1.52}$, (c, g, k) $Zr_{0.68}Cr_{0.32}B_{1.38}$, and (d, h, l) $Zr_{0.56}Cr_{0.44}B_{1.11}$ thin films grown on Si(001) substrates. The corresponding SAED patterns are given in insets. The high-resolution BF-XTEM image of $Zr_{0.56}Cr_{0.44}B_{1.11}$ is shown as inset in (h). The brightness appearing at the substrate/film interfaces in XSEM images of $Zr_{0.77}Cr_{0.23}B_{1.52}$ and $Zr_{0.68}Cr_{0.32}B_{1.38}$ films originates from charging.

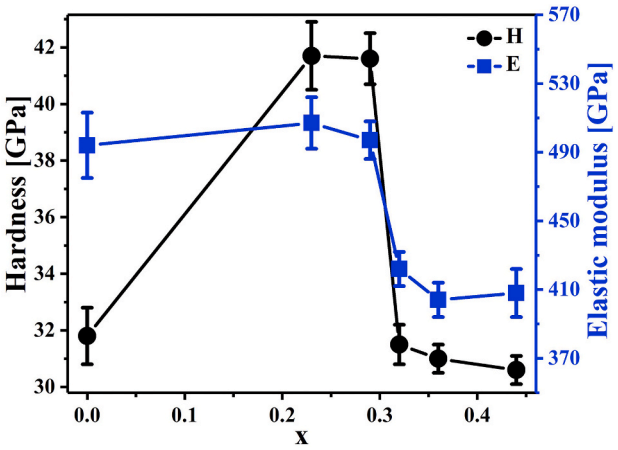

Fig. 4. Nanoindentation hardness H and elastic modulus E of as-deposited $Zr_{1-x}Cr_xB_y$ thin films grown on $Al_2O_3(0001)$ substrates as a function of x ranging from 0 to 0.44.

$Zr_{0.56}Cr_{0.44}B_{1.11}$ alloys. Fig. 5 compares the SEM images of the cube-corner nanoindentations made by a load of 200 mN. The average length of radial cracks induced by 200 mN significantly decreases from $C_m = 4260 \pm 200$ nm for $ZrB_{2.18}$, to 2050 ± 190 nm for $Zr_{0.77}Cr_{0.23}B_{1.52}$, 1370 ± 110 nm for $Zr_{0.68}Cr_{0.32}B_{1.38}$, and 720 ± 64 nm for $Zr_{0.56}Cr_{0.44}B_{1.11}$ films. Spalling, which is a common characteristic of indented brittle materials, can be observed around the nanoindentations of $ZrB_{2.18}$ and $Zr_{0.77}Cr_{0.23}B_{1.52}$, while there is a significant pileup around the nanoindentations of $Zr_{0.68}Cr_{0.32}B_{1.38}$ and $Zr_{0.56}Cr_{0.44}B_{1.11}$, proving a higher ductility for these alloys.

The adhesion strengths of as-deposited $ZrB_{2.18}$, $Zr_{0.77}Cr_{0.23}B_{1.52}$, $Zr_{0.68}Cr_{0.32}B_{1.38}$, and $Zr_{0.56}Cr_{0.44}B_{1.11}$ thin films grown on WC-Co substrates are evaluated by Revescratch tests. Optical microscope images from the scratch tracks, together with corresponding SEM micrographs acquired from the regions indicated by dashed and solid boxes in the optical microscope images, are exhibited in Fig. 6. The optical microscope images show that all films follow a similar scratch-failure mode; starting with chips spallation on the side of tracks, then wedge spallation, and eventually substrates exposure, which are the common failure modes observed for hard thin films [50,51]. The minimum load at which peeling and spallation occurs, referred to as the critical load (L_{c2}) [52], is considered as the representative of adhesive failure, i.e. film delamination and spallation. The $ZrB_{2.18}$ film exhibits a poor adhesion together with severe chipping and buckling along its scratch track, with $L_{c2} = \sim 29$ N, due to its high brittleness. Although the L_{c2} value of the $Zr_{0.77}Cr_{0.23}B_{1.52}$ alloys (~28 N) is almost similar to that of $ZrB_{2.18}$, it increases significantly to ~42 and ~49 N for $Zr_{0.68}Cr_{0.32}B_{1.38}$ and $Zr_{0.56}Cr_{0.44}B_{1.11}$, respectively. The SEM images from the regions indicated with dashed boxes, at distances between ~1.0 mm and ~1.1 mm (~30 N), in the optical microscope images of $ZrB_{2.18}$ and $Zr_{0.68}Cr_{0.32}B_{1.38}$ reveal angular cracks (indicated with black arrows) appeared close to the scratch tracks, which form due to their tensile stresses [51,53]. However, the SEM images of the $Zr_{0.77}Cr_{0.23}B_{1.52}$ and $Zr_{0.56}Cr_{0.44}B_{1.11}$ thin films, from the same distances (~1.0 to ~1.1 mm), do not show such angular cracks as they have compressive stresses.

The reduction in chipping debris observed for $Zr_{0.68}Cr_{0.32}B_{1.38}$ and $Zr_{0.56}Cr_{0.44}B_{1.11}$, compared to $ZrB_{2.18}$ and $Zr_{0.77}Cr_{0.23}B_{1.52}$, confirms the increase in the film toughness. While the most striking surface feature in the SEM images from the regions at distances between ~1.0 mm and ~1.1 mm is peeling and spallation for $ZrB_{2.18}$ and $Zr_{0.77}Cr_{0.23}B_{1.52}$, the SEM images of $Zr_{0.68}Cr_{0.32}B_{1.38}$ and $Zr_{0.56}Cr_{0.44}B_{1.11}$ from similar distances, dashed boxes, do not indicate any obvious change in the microstructure of scratched surfaces. Compared to the SEM images of $ZrB_{2.18}$ and $Zr_{0.77}Cr_{0.23}B_{1.52}$ acquired from the L_{c2} regions primarily showing chipping debris, the SEM micrographs of $Zr_{0.68}Cr_{0.32}B_{1.38}$ and

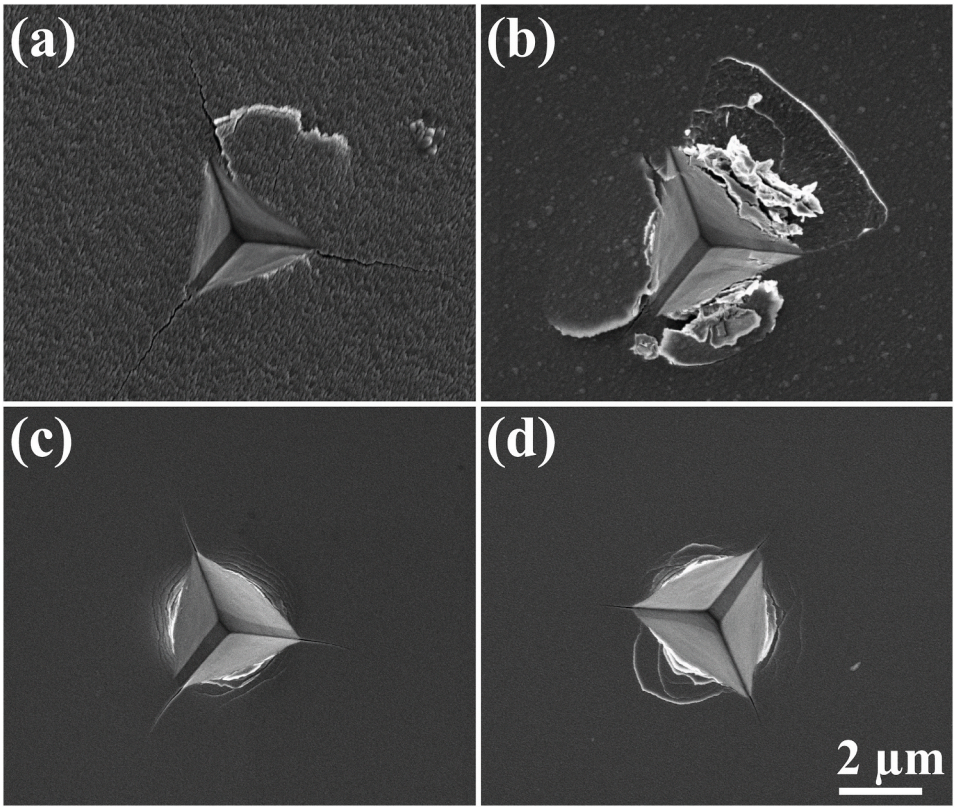

Fig. 5. SEM images from the cube-corner nanoindentations of as-deposited (a) $ZrB_{2.18}$, (b) $Zr_{0.77}Cr_{0.23}B_{1.52}$, (c) $Zr_{0.68}Cr_{0.32}B_{1.38}$, and (d) $Zr_{0.56}Cr_{0.44}B_{1.11}$ thin films grown on $Al_2O_3(0001)$ substrates made with a load of 200 mN.

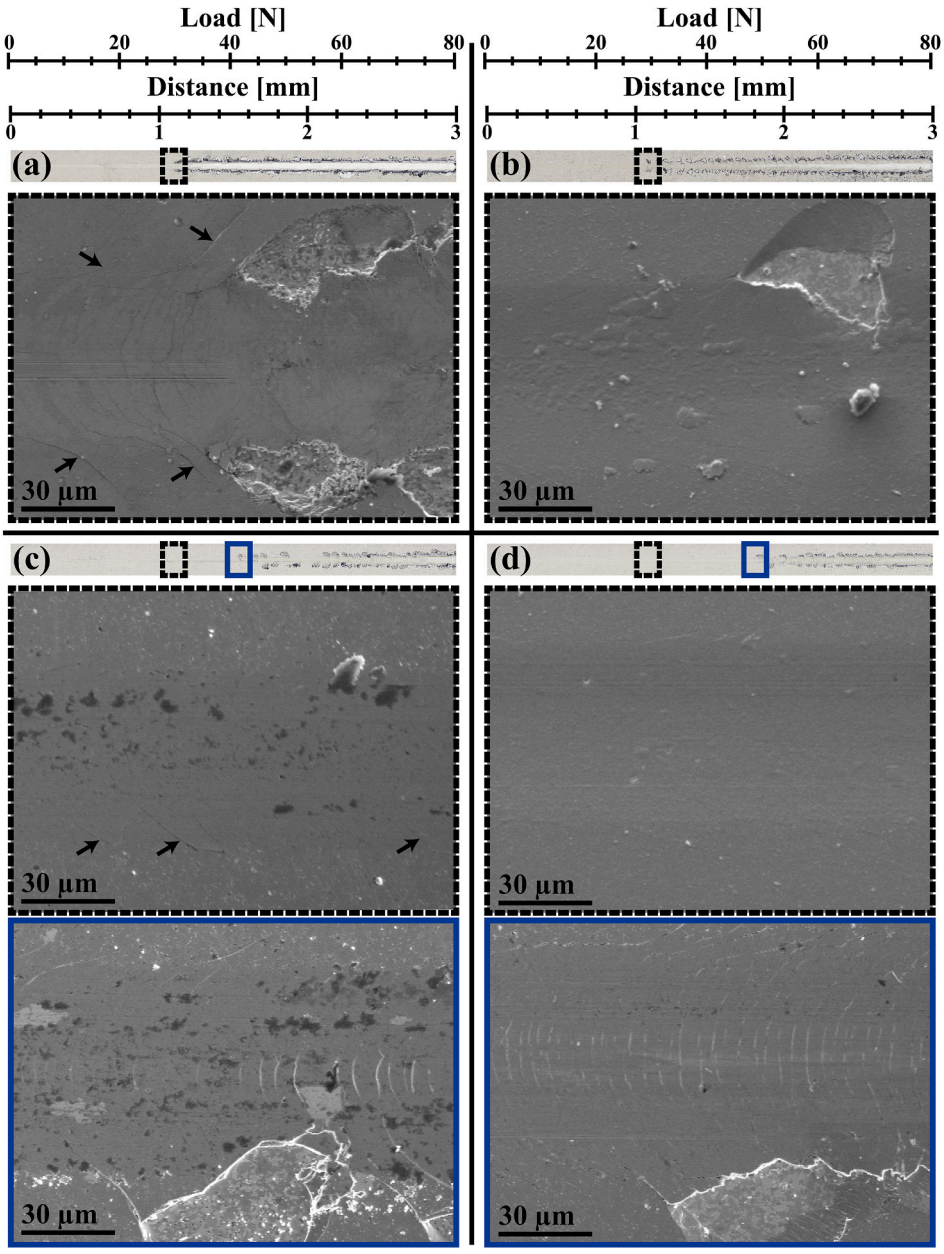

Fig. 6. Optical microscope images from the scratch tracks of as-deposited (a) $ZrB_{2.18}$, (b) $Zr_{0.77}Cr_{0.23}B_{1.52}$, (c) $Zr_{0.68}Cr_{0.32}B_{1.38}$, and (d) $Zr_{0.56}Cr_{0.44}B_{1.11}$ thin films grown on WC-Co substrates. SEM images show the regions indicated by dashed and solid boxes in the optical microscope images of the scratch tracks.

$Zr_{0.56}Cr_{0.44}B_{1.11}$ alloys obtained from their L_{c2} regions, indicated by blue solid boxes in their optical microscope images, consist of chipping debris and transverse semicircular cracks appeared in the scratch tracks, an indication of plastic deformation [51].

The friction coefficients (μ) and wear rates of as-deposited $ZrB_{2.18}$, $Zr_{0.77}Cr_{0.23}B_{1.52}$, $Zr_{0.68}Cr_{0.32}B_{1.38}$, and $Zr_{0.56}Cr_{0.44}B_{1.11}$ thin films grown on WC-Co substrates are given in Table 2. Optical microscope images from the wear tracks of these layers are also compared in Fig. 7. The friction coefficient is 0.518 ± 0.004 for $ZrB_{2.18}$, 0.538 ± 0.007 for $Zr_{0.77}Cr_{0.23}B_{1.52}$, 0.565 ± 0.007 for $Zr_{0.68}Cr_{0.32}B_{1.38}$, and 0.522 ± 0.007 for $Zr_{0.56}Cr_{0.44}B_{1.11}$. The results show that adding Cr does not have a significant influence on the friction coefficients of the $Zr_{1-x}Cr_xB_y$ alloys. However, the wear resistance of $ZrB_{2.18}$ thin films is considerably improved by alloying with Cr. The wear rate decreases from (7.9 ± 0.4) × 10^{-16} m^3/(Nm) for $ZrB_{2.18}$, to (2.5 ± 0.3) × 10^{-16} m^3/(Nm) for $Zr_{0.77}Cr_{0.23}B_{1.52}$, (2.1 ± 0.2) × 10^{-16} m^3/(Nm) for $Zr_{0.68}Cr_{0.32}B_{1.38}$, and (0.6 ± 0.1) × 10^{-16} m^3/(Nm) for $Zr_{0.56}Cr_{0.44}B_{1.11}$.

Table 2
Friction coefficients (μ) and wear rates of as-deposited $ZrB_{2.18}$, $Zr_{0.77}Cr_{0.23}B_{1.52}$, $Zr_{0.68}Cr_{0.32}B_{1.38}$, and $Zr_{0.56}Cr_{0.44}B_{1.11}$ thin films grown on WC-Co substrates.

Films	μ [a.u.]	Wear rate [× 10^{-16} m^3/(Nm)]
$ZrB_{2.18}$	0.518 ± 0.004	7.9 ± 0.4
$Zr_{0.77}Cr_{0.23}B_{1.52}$	0.538 ± 0.007	2.5 ± 0.3
$Zr_{0.68}Cr_{0.32}B_{1.38}$	0.565 ± 0.007	2.1 ± 0.2
$Zr_{0.56}Cr_{0.44}B_{1.11}$	0.522 ± 0.007	0.6 ± 0.1

The broad wear track of $ZrB_{2.18}$, Fig.7(a), shows a higher material loss (i.e. higher wear rate) occurring during the wear test with a typical wear caused by plastic deformation. There is a decrease in the width of wear tracks as a function of Cr concentration in the alloys. Compared to $ZrB_{2.18}$, the adhesive wear is the primary wear mechanism of as-deposited $Zr_{1-x}Cr_xB_y$ thin films, Figs. 7(b), (c), and 7(d). The adhesion of the alloys to the GCr15 steel produces a high material loss of the friction ball, instead of the alloys, which reduces the wear rate. The

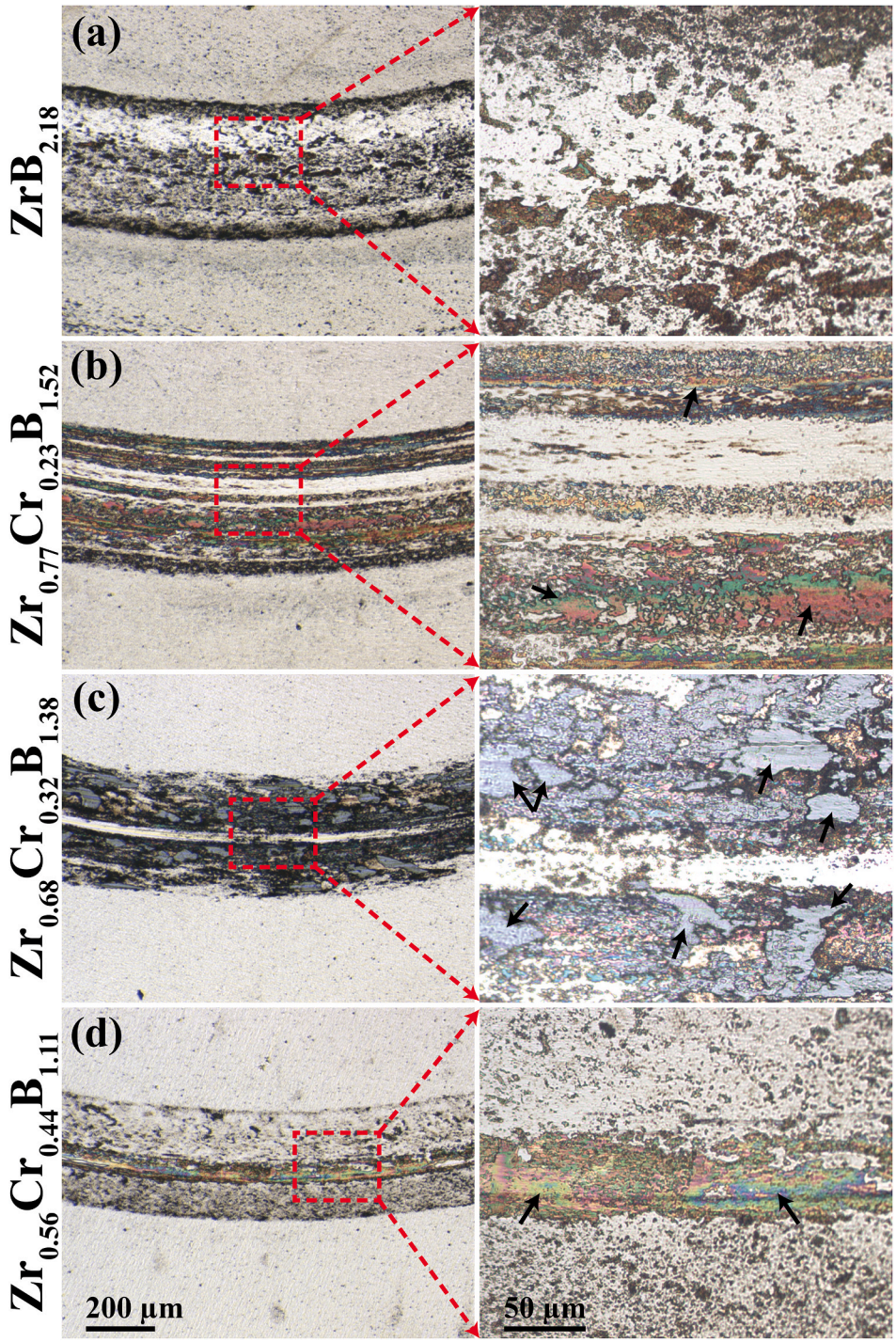

Fig. 7. Optical microscope images from the wear tracks of as-deposited (a) $ZrB_{2.18}$, (b) $Zr_{0.77}Cr_{0.23}B_{1.52}$, (c) $Zr_{0.68}Cr_{0.32}B_{1.38}$, and (d) $Zr_{0.56}Cr_{0.44}B_{1.11}$ thin films grown on WC-Co substrates. The arrows in the right images, which are magnified regions indicated with dashed boxes in (a) to (d), show adhered GCr15 steel traces on the wear tracks.

enhanced wear resistance can be attributed to the combination of high hardness (>30 GPa) and increased toughness.

Out of all compositions investigated, $Zr_{0.56}Cr_{0.44}B_{1.11}$ alloys are chosen for further oxidation and corrosion studies as they have metallic-glass structure, relatively low residual stress, good hardness and toughness, and the highest wear resistance.

3.3. Oxidation properties

Fig. 8 compares the XSEM images of ~2800-nm $ZrB_{2.18}$ and ~2100-nm $Zr_{0.56}Cr_{0.44}B_{1.11}$ thin films annealed in air at 700 °C for the time t_a of 1, 3, and 5 h. The thickness of the oxide scale on $ZrB_{2.18}$ increases from 830 ± 50 nm for t_a = 1 h, to 2620 ± 80 nm for t_a = 3 h, and 3460 ± 90 nm for t_a = 5 h. The oxide-scale thickness changes linearly as a function of oxidation time ($d_{ox} = 708 \cdot t_a + 135$). However, the oxide scales formed on the $Zr_{0.56}Cr_{0.44}B_{1.11}$ alloys are significantly thinner than those on $ZrB_{2.18}$ over the entire t_a range. The thickness of the oxide scale on $Zr_{0.56}Cr_{0.44}B_{1.11}$ increases from 350 ± 30 nm for t_a = 1 h, to 550 ± 50 nm for t_a = 3 h, and 665 ± 55 nm for t_a = 5 h, following a $d_{ox} = 352.4 \cdot t_a^{0.4}$ relationship.

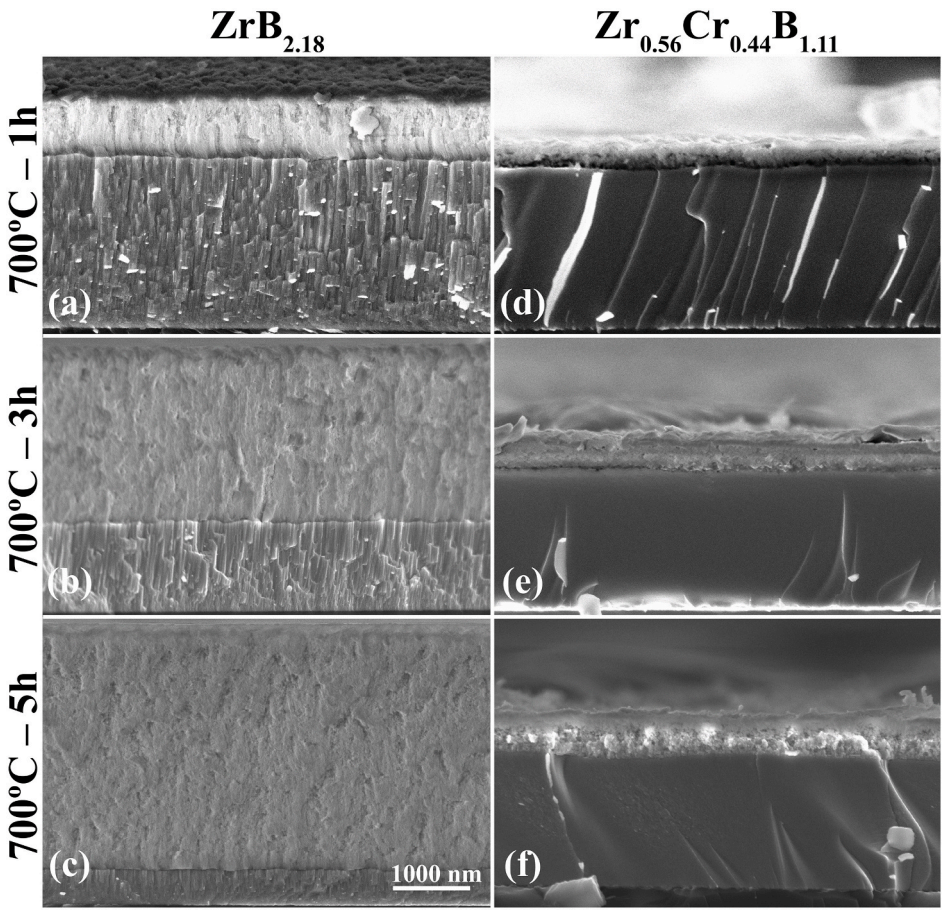

Fig. 8. XSEM images of $ZrB_{2.18}$ and $Zr_{0.56}Cr_{0.44}B_{1.11}$ thin films annealed at 700 °C for (a and d) 1 h, (b and e) 3 h, and (c and f) 5 h. The films are grown on Si(001) substrates. From the phase diagrams, Si has less affinity to the boride components than Al and O; thus, Si substrates are the better choice to elucidate the role of oxidation. The scale bar is the same for all panels.

The enhanced oxidation resistance observed for the $Zr_{0.56}Cr_{0.44}B_{1.11}$ alloys is attributed to their elemental composition and nanostructure. The TMB_2 oxidation, which is mainly influenced by the evaporation rate of B_2O_3 (*g*) phase, largely depends on the oxygen partial pressure, annealing temperature, and B concentration [11,54]. At constant oxygen partial pressure and annealing temperature, the vapor pressure of the B_2O_3 (*g*) phase increases as a function of B concentration that results in decreasing the oxidation resistance [54]. We recently showed that sputter-deposited columnar $TiB_{2.4}$ thin films, in which the excess B segregates to the column boundaries, are highly prone to continuous vigorous oxidation in air [16]. The B_2O_3 (*g*) phase preferentially forms at the column boundaries, which are B-rich, during annealing at temperatures above 400 °C. The evaporation of this phase, together with the coarsening of TiO_2 (*s*), lead to the formation of large gaps between the TiO_2 (*s*) columns that act as wide channels for oxygen to readily access the unoxidized regions; consequently, causing a continuous oxidation [16]. Hence, the higher oxidation resistance of $Zr_{0.56}Cr_{0.44}B_{1.11}$ can be explained by its very-low B concentration and amorphous structure, where the alloy does not have the B-rich column boundaries that are susceptible to preferential oxidation.

In addition, Lee et al. [28] showed that the oxidation resistance of $Ti_{1-x}Cr_xN$ films, isothermally annealed from 700 to 1000 °C in air, increases as a function of Cr concentration. The oxide scales formed on these alloys mainly consist of TiO_2 (*s*) and Cr_2O_3 (*s*) phases [27,28]. As the Cr_2O_3 (*s*) phase has a significantly lower coarsening rate than TiO_2 (*s*) [55], alloying TiN films with Cr decreases the coarsening of the oxide scale, which leads to suppressing the porosity formation and hence, decreasing the oxygen diffusion through the scale. This results in enhancing the oxidation resistance of $Ti_{1-x}Cr_xN$ films. Similar effect can be expected for the $Zr_{0.56}Cr_{0.44}B_{1.11}$ alloys.

3.4. Corrosion properties

The corrosion properties of as-deposited $ZrB_{2.18}$ and $Zr_{0.56}Cr_{0.44}B_{1.11}$ thin films grown on WC-Co substrates are obtained by electrochemical measurements during the immersion of the layers in the 0.1 M NaCl corrosive medium for 25 h, at room temperature and without agitation. The open circuit potential (E_{ocp}), linear polarization resistance (R_p), and potentiodynamic polarization curves of $ZrB_{2.18}$ and $Zr_{0.56}Cr_{0.44}B_{1.11}$ thin films are shown in Fig. 9. The electrochemical data determined from the polarization curves are summarized in Tables 3 and 4. Fig. 9(a) compares the E_{ocp} values of $ZrB_{2.18}$ and $Zr_{0.56}Cr_{0.44}B_{1.11}$ as a function of immersion time (t_{ocp}). The low-intensity peaks in these curves result from the R_p measurements at $t_{ocp} = 0.25$, 0.5, 1.0, 2.0, 4.0, 8.0, 16.0, and 24.0 h. Both films have negative E_{ocp} values over the entire t_{ocp} range. The open circuit potential of $ZrB_{2.18}$ continuously decreases from −180 ± 28 mV for $t_{ocp} = 0.25$ h to −230 ± 18 mV for $t_{ocp} = 16.0$ h and then reaches an almost stable potential (∼−230 mV). However, the $Zr_{0.56}Cr_{0.44}B_{1.11}$ films achieve a relatively stable E_{ocp} of ∼ −150 mV after 2.0 h immersing in the corrosive medium. In general, the $Zr_{0.56}Cr_{0.44}B_{1.11}$ alloys have lower negative E_{ocp} values, i.e. more noble, than the $ZrB_{2.18}$ films over the entire t_{ocp} range. This reveals that the $Zr_{0.56}Cr_{0.44}B_{1.11}$ films have a better electrochemical stability in the 0.1 M NaCl medium compared to $ZrB_{2.18}$ [56].

Fig. 9(b) exhibits the R_p values of as-deposited $ZrB_{2.18}$ and $Zr_{0.56}Cr_{0.44}B_{1.11}$ thin films determined at times ranging from 0.25 to

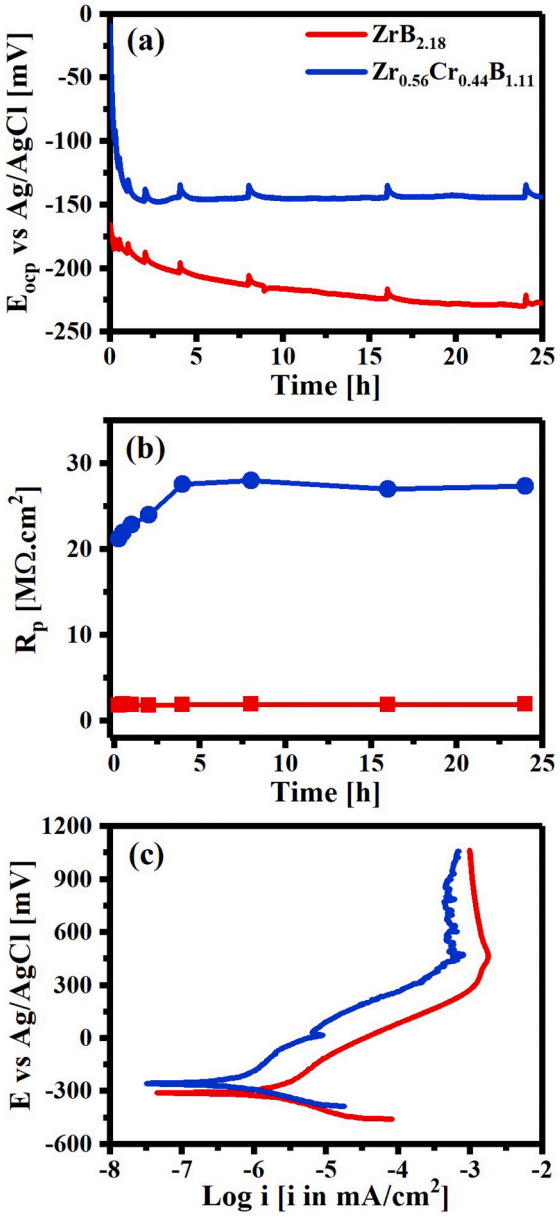

Fig. 9. (a) Open circuit potential (E_{ocp}), (b) linear polarization resistance (R_p), and (c) potentiodynamic polarization curves of $ZrB_{2.18}$ and $Zr_{0.56}Cr_{0.44}B_{1.11}$ thin films grown on WC-Co substrates. The measurements are carried out in the aqueous 0.1 M NaCl corrosive medium, at room temperature and without agitation.

Table 3
Open circuit potential (E_{ocp}) and linear polarization resistance (R_p) of $ZrB_{2.18}$ and $Zr_{0.56}Cr_{0.44}B_{1.11}$ thin films. The measurements are carried out in the aqueous 0.1 M NaCl corrosive medium, at room temperature and without agitation.

Time [h]	E_{ocp} [mV]		R_p [MΩ.cm^2]	
	$ZrB_{2.18}$	$Zr_{0.56}Cr_{0.44}B_{1.11}$	$ZrB_{2.18}$	$Zr_{0.56}Cr_{0.44}B_{1.11}$
0.25	−180 ± 28	−109 ± 21	2.0 ± 0.3	16.0 ± 5.1
0.5	−180 ± 22	−124 ± 20	2.1 ± 0.2	19.2 ± 4.1
1.0	−190 ± 19	−149 ± 32	2.1 ± 0.3	20.4 ± 4.5
2.0	−200 ± 16	−146 ± 18	2.2 ± 0.3	20.7 ± 4.2
4.0	−210 ± 14	−148 ± 15	2.2 ± 0.3	23.3 ± 5.3
8.0	−220 ± 17	−151 ± 7	2.1 ± 0.2	25.6 ± 3.4
16.0	−230 ± 18	−151 ± 5	2.2 ± 0.3	27.0 ± 3.8
24.0	−230 ± 17	−149 ± 3	2.2 ± 0.3	27.3 ± 2.9

Table 4
Corrosion potential (E_{corr}), corrosion current density (i_{corr}), and passive current density (i_{pass}) obtained from the potentiodynamic polarization curves of $ZrB_{2.18}$ and $Zr_{0.56}Cr_{0.44}B_{1.11}$ thin films determined after 25 h immersing in the aqueous 0.1 M NaCl corrosive medium, at room temperature and without agitation.

Films	E_{corr} [mV]	i_{corr} [× 10^{-6} mA/cm^2]	i_{pass} [× 10^{-3} mA/cm^2]
$ZrB_{2.18}$	−250 ± 49	4.6 ± 2.0	1.3 ± 0.3
$Zr_{0.56}Cr_{0.44}B_{1.11}$	−180 ± 59	0.54 ± 0.1	0.6 ± 0.1

24.0 h. The alloys have significantly higher R_p values than the $ZrB_{2.18}$ films (see Table 3); the R_p value of $Zr_{0.56}Cr_{0.44}B_{1.11}$ obtained after a 24.0-h immersion in the corrosive medium is about twelve times higher than that of $ZrB_{2.18}$ (2.2 ± 0.3 MΩ cm^2 for $ZrB_{2.18}$ and 27.3 ± 2.9 MΩ cm^2 for $Zr_{0.56}Cr_{0.44}B_{1.11}$). Comparing the potentiodynamic polarization curves acquired after 25.0 h, Fig. 9(c), indicates that the $Zr_{0.56}Cr_{0.44}B_{1.11}$ alloys have lower corrosion current densities (i_{corr}) than the reference $ZrB_{2.18}$ films. The i_{corr} value decreases from (4.6 ± 2.0) × 10^{-6} mA/cm^2 for $ZrB_{2.18}$ to (0.54 ± 0.1) × 10^{-6} mA/cm^2 for $Zr_{0.56}Cr_{0.44}B_{1.11}$ at the E_{corr} values of −250 ± 49 mV and −180 ± 59 mV, respectively. This indicates that the corrosion rate of $Zr_{0.56}Cr_{0.44}B_{1.11}$ is almost nine times lower than that of $ZrB_{2.18}$. The anodic polarization curves of both films consist of passive regions (from ~450 to ~1050 mV), where the one for $Zr_{0.56}Cr_{0.44}B_{1.11}$ is to some extent metastable, but at lower anodic current densities compared to that for $ZrB_{2.18}$. The passive current density i_{pass} is (1.3 ± 0.3) × 10^{-3} mA/cm^2 for $ZrB_{2.18}$ and (0.6 ± 0.1) × 10^{-3} mA/cm^2 for $Zr_{0.56}Cr_{0.44}B_{1.11}$.

Alloying directly influences on the corrosion properties of materials by changing their nobility [56–58]. The lower E_{ocp} value obtained for $Zr_{0.56}Cr_{0.44}B_{1.11}$ demonstrates that the electrochemical stability of these alloys is higher than that of $ZrB_{2.18}$ as Cr is a more noble element. The other factors that effectively change the corrosion resistance are the column boundaries and their density [59,60]. The column boundaries of $ZrB_{2.18}$ are more prone to corrosion attack than inside the columns, due to heterogeneity in their structure and chemistry (e.g. the B-rich phase). Thus, the absence of column boundaries for amorphous $Zr_{0.56}Cr_{0.44}B_{1.11}$ may contribute to a better corrosion resistance compared to that for polycrystalline $ZrB_{2.18}$ [61].

4. Conclusions

We demonstrate control of the composition, nanostructure, and properties of ZrB_2-rich $Zr_{1-x}Cr_xB_y$ films grown by hybrid Cr-HiPIMS/ZrB_2-DCMS co-sputtering. The reference $ZrB_{2.18}$ layers are deposited by DCMS with a negative dc substrate bias of 100 V. For the $Zr_{1-x}Cr_xB_y$ alloy growth, the ZrB_2 target is continuously sputtered by DCMS, while the Cr magnetron is operated in HiPIMS mode providing pulsed Cr-ion fluxes. The Cr metal fraction, Cr/(Zr + Cr), is increased from x = 0.23 to x = 0.44 by decreasing the power P_{ZrB_2} applied to the DCMS ZrB_2 target from 4000 to 2000 W in 500-W increments, while the average power, pulse width, and frequency applied to the HiPIMS Cr target are maintained constant at 700 W, 50 μs, and 100 Hz, respectively. Concurrently, y decreases from 2.18 to 1.11 as a function of P_{ZrB_2}, due both to the addition of Cr (primarily) and preferential B resputtering. The energetic Cr-ion bombardment increases the density of the alloys and causes re-nucleation of the column growth. As a result, there is a refinement of the columnar structure with increasing the Cr concentration accompanied by increasing hardness to ~42 GPa for $Zr_{0.77}Cr_{0.23}B_{1.52}$ and $Zr_{0.71}Cr_{0.29}B_{1.42}$. However, the further increase of Cr concentration leads to a significant B deficiency that results in the collapse of the hexagonal AlB_2-structure into amorphous dense alloys, as revealed by XRD, TEM, and SAED patterns, with hardness values above 30 GPa.

The changes in the composition and nanostructure result in enhanced toughness and wear properties. The $Zr_{0.56}Cr_{0.44}B_{1.11}$ alloys, with the highest Cr concentration, exhibit considerably better toughness and wear resistance compared to $ZrB_{2.18}$. The wear rate decreases from

~7.9 × 10^{-16} m^3/(Nm) for $ZrB_{2.18}$ to ~0.6 × 10^{-16} m^3/(Nm) for $Zr_{0.56}Cr_{0.44}B_{1.11}$. In addition, these alloy films exhibit significantly higher oxidation and corrosion resistance. The thickness of oxide scale formed after air-annealing at 700 °C for 5.0 h markedly decreases from ~3460 nm for $ZrB_{2.18}$ to ~665 nm for $Zr_{0.56}Cr_{0.44}B_{1.11}$. The corrosion rate of $Zr_{0.56}Cr_{0.44}B_{1.11}$ is about nine times lower than $ZrB_{2.18}$. The $Zr_{0.56}Cr_{0.44}B_{1.11}$ alloys with the structural characteristics of metallic-glass thin films show simultaneously several enhanced properties, which are essential for many strategic applications.

Declaration of competing interest

The authors declare that they have no known competing financial interests or personal relationships that could have appeared to influence the work reported in this paper.

Acknowledgments

We acknowledge support from the Knut and Alice Wallenberg (KAW) foundation for Project funding (KAW 2015.0043). Financial support from the Swedish Research Council VR Grant 2018–03957 and 642-2013-8020, the VINNOVA Grant 2019–04882, and Carl Tryggers Stiftelse contracts CTS 15:219, CTS 20:150, and CTS 14:431 are also gratefully acknowledged. Furthermore, the authors acknowledge financial support from the Swedish Government Strategic Research Area in Materials Science on Functional Materials at Linköping University (Faculty Grant SFO Mat LiU No. 2009 00971). Supports from the Swedish research council VR-RFI (#2017–00646_9) for the Accelerator based ion-technological center and from the Swedish Foundation for Strategic Research (contract RIF14-0053; for the tandem accelerator laboratory in Uppsala University, and contract RIF14-0074; for the electron microscopy laboratory) are acknowledged.

References

[1] T. Leyendecker, O. Lemmer, S. Esser, J. Ebberink, The development of the PVD coating TiAlN as a commercial coating for cutting tools, Surf. Coating. Technol. 48 (2) (1991) 175–178.
[2] B. Subramanian, C.V. Muraleedharan, R. Ananthakumar, M. Jayachandran, A comparative study of titanium nitride (TiN), titanium oxy nitride (TiON) and titanium aluminum nitride (TiAlN), as surface coatings for bio implants, Surf. Coating. Technol. 205 (21) (2011) 5014–5020.
[3] L.E. Toth, Transition Metal Carbides and Nitrides, Academic Press, NY, 1971.
[4] O. Knotek, M. Böhmer, T. Leyendecker, On structure and properties of sputtered Ti and Al based hard compound films, J Vac. Sci. Technol. A 4 (6) (1986) 2695–2700.
[5] R. Rachbauer, S. Massl, E. Stergar, D. Holec, D. Kiener, J. Keckes, J. Patscheider, M. Stiefel, H. Leitner, P.H. Mayrhofer, Decomposition pathways in age hardening of Ti-Al-N films, J. Appl. Phys. 110 (2) (2011), 023515.
[6] N.P. Bansal, Handbook of Ceramic Composites, Kluwer Academic Publishers, Boston MA, 2005.
[7] N.L. Okamoto, M. Kusakari, K. Tanaka, H. Inui, S. Otani, Anisotropic elastic constants and thermal expansivities in monocrystal CrB_2, TiB_2, and ZrB_2, Acta Mater. 58 (1) (2010) 76–84.
[8] V.I. Matkovich, G.V. Samsonov, P. Hagenmuller, T. Lundstrom, Boron and Refractory Borides, Springer-Verlag, Berlin, 1977.
[9] L. Bsenko, T. Lundström, The high-temperature hardness of ZrB_2 and HfB_2, J Less Common Met 34 (2) (1974) 273–278.
[10] V. Moraes, C. Fuger, V. Paneta, D. Primetzhofer, P. Polcik, H. Bolvardi, M. Arndt, H. Riedl, P.H. Mayrhofer, Substoichiometry and tantalum dependent thermal stability of α-structured W-Ta-B thin films, Scripta Mater. 155 (2018) 5–10.
[11] W.G. Fahrenholtz, G.E. Hilmas, Ultra-high temperature ceramics: materials for extreme environments, Scripta Mater. 129 (2017) 94–99.
[12] F. Monteverde, L. Scatteia, Resistance to thermal shock and to oxidation of metal diborides-SiC ceramics for aerospace application, J. Am. Ceram. Soc. 90 (4) (2007) 1130–1138.
[13] G. Sade, J. Pelleg, Co-sputtered TiB_2 as a diffusion barrier for advanced microelectronics with Cu metallization, Appl. Surf. Sci. 91 (1) (1995) 263–268.
[14] J. Sung, D.M. Goedde, G.S. Girolami, J.R. Abelson, Remote-plasma chemical vapor deposition of conformal ZrB_2 films at low temperature: a promising diffusion barrier for ultralarge scale integrated electronics, J. Appl. Phys. 91 (6) (2002) 3904–3911.
[15] E. Sani, M. Meucci, L. Mercatelli, A. Balbo, C. Musa, R. Licheri, R. Orrù, G. Cao, Titanium diboride ceramics for solar thermal absorbers, Sol. Energy Mater. Sol. Cells 169 (2017) 313–319.
[16] B. Bakhit, J. Palisaitis, J. Thörnberg, J. Rosen, P.O.Å. Persson, L. Hultman, I. Petrov, J.E. Greene, G. Greczynski, Improving the high-temperature oxidation resistance of TiB_2 thin films by alloying with Al, Acta Mater. 196 (2020) 677–689.
[17] B. Bakhit, D.L.J. Engberg, J. Lu, J. Rosen, H. Högberg, L. Hultman, I. Petrov, J. E. Greene, G. Greczynski, Strategy for simultaneously increasing both hardness and toughness in ZrB_2-rich $Zr_{1-x}Ta_xB_y$ thin films, J Vac. Sci. Technol. A 37 (3) (2019), 031506.
[18] B. Bakhit, J. Palisaitis, P.O.Å. Persson, B. Alling, J. Rosen, L. Hultman, I. Petrov, J. E. Greene, G. Greczynski, Self-organized columnar $Zr_{0.7}Ta_{0.3}B_{1.5}$ core/shell-nanostructure thin films, Surf. Coating. Technol. 401 (2020), 126237.
[19] B. Bakhit, I. Petrov, J.E. Greene, L. Hultman, J. Rosén, G. Greczynski, Controlling the B/Ti ratio of TiB_x thin films grown by high-power impulse magnetron sputtering, J Vac. Sci. Technol. A 36 (3) (2018), 030604.
[20] B. Bakhit, J. Palisaitis, Z. Wu, M.A. Sortica, D. Primetzhofer, P.O.Å. Persson, J. Rosen, L. Hultman, I. Petrov, J.E. Greene, G. Greczynski, Age hardening in superhard ZrB_2-rich $Zr_{1-x}Ta_xB_y$ thin films, Scripta Mater. 191 (2021) 120–125.
[21] W.G. Fahrenholtz, G.E. Hilmas, I.G. Talmy, J.A. Zaykoski, Refractory diborides of zirconium and hafnium, J. Am. Ceram. Soc. 90 (5) (2007) 1347–1364.
[22] T.A. Parthasarathy, R.A. Rapp, M. Opeka, R.J. Kerans, A model for the oxidation of ZrB_2, HfB_2 and TiB_2, Acta Mater. 55 (17) (2007) 5999–6010.
[23] A. Kirnbauer, A. Wagner, V. Moraes, D. Primetzhofer, M. Hans, J.M. Schneider, P. Polcik, P.H. Mayrhofer, Thermal stability and mechanical properties of sputtered (Hf,Ta,V,W,Zr)-diborides, Acta Mater. 200 (2020) 559–569.
[24] P.H. Mayrhofer, C. Mitterer, J.G. Wen, J.E. Greene, I. Petrov, Self-organized nanocolumnar structure in superhard TiB_2 thin films, Appl. Phys. Lett. 86 (13) (2005), 131909.
[25] W.J. Clegg, Controlling cracks in ceramics, Science 286 (5442) (1999), 1097.
[26] R.O. Ritchie, The conflicts between strength and toughness, Nat. Mater. 10 (11) (2011) 817–822.
[27] Y. Otani, S. Hofmann, High temperature oxidation behaviour of $(Ti_{1-x}Cr_x)N$ coatings, Thin Solid Films 287 (1) (1996) 188–192.
[28] D.B. Lee, M.H. Kim, Y.C. Lee, S.C. Kwon, High temperature oxidation of TiCrN coatings deposited on a steel substrate by ion plating, Surf. Coating. Technol. 141 (2) (2001) 232–239.
[29] S.M. Aouadi, K.C. Wong, K.A.R. Mitchell, F. Namavar, E. Tobin, D.M. Mihut, S. L. Rohde, Characterization of titanium chromium nitride nanocomposite protective coatings, Appl. Surf. Sci. 229 (1) (2004) 387–394.
[30] K.H. Lee, C.H. Park, Y.S. Yoon, H.A. Jehn, J.J. Lee, Wear and corrosion properties of $(Ti_{1-x}Cr_x)N$ coatings produced by the ion-plating method, Surf. Coating. Technol. 142–144 (2001) 971–977.
[31] Z.G. Zhang, O. Rapaud, N. Bonasso, D. Mercs, C. Dong, C. Coddet, Microstructures and corrosion behaviors of Zr modified CrN coatings deposited by DC magnetron sputtering, Vacuum 82 (11) (2008) 1332–1336.
[32] G. Greczynski, I. Petrov, J.E. Greene, L. Hultman, Paradigm shift in thin-film growth by magnetron sputtering: from gas-ion to metal-ion irradiation of the growing film, J Vac. Sci. Technol. A 37 (6) (2019), 060801.
[33] G. Greczynski, L. Hultman, X-ray photoelectron spectroscopy: towards reliable binding energy referencing, Prog. Mater. Sci. 107 (2020), 100591.
[34] W.C. Oliver, G.M. Pharr, An improved technique for determining hardness and elastic modulus using load and displacement sensing indentation experiments, J. Mater. Res. 7 (6) (1992) 1564–1583.
[35] S. Zhang, D. Sun, Y. Fu, H. Du, Toughness measurement of thin films: a critical review, Surf. Coating. Technol. 198 (1) (2005) 74–84.
[36] I. Kraghelsky, Calculation of wear rate, J Basic Eng 87 (3) (1965) 785–790.
[37] J. Tafel, Über die Polarisation bei kathodischer Wasserstoffentwicklung, Z. Phys. Chem. 50 (1905), 641.
[38] E. McCafferty, Validation of corrosion rates measured by the Tafel extrapolation method, Corrosion Sci. 47 (12) (2005) 3202–3215.
[39] JCPDS International Centre for Diffraction Data. Zirconium diboride(ZrB_2) Card00-034-0423.
[40] JCPDS International Centre for Diffraction Data. Chromium diboride(CrB_2) Card00-008-0119.
[41] W. Martienssen, H. Warlimont, Springer Handbook of Condensed Matter and Materials Data, Springer, Heidelberg, Berlin, 2006.
[42] P. Zaumseil, High-resolution characterization of the forbidden Si 200 and Si 222 reflections, J. Appl. Crystallogr. 48 (2) (2015) 528–532.
[43] L. Pauling, The nature of the chemical bond, IV. The energy of single bonds and the relative electronegativity of atoms, J. Am. Chem. Soc. 54 (9) (1932) 3570–3582.
[44] A. Arranz, C. Palacio, Screening effects in the Ti 2p core level spectra of Ti-based ternary nitrides, Surf. Sci. 600 (12) (2006) 2510–2517.
[45] G.E. Dieter, D.J. Bacon, Mechanical Metallurgy, McGraw-hill, NY, 1986.
[46] E.O. Hall, The deformation and ageing of mild steel: III discussion of results, Proc. Phys. Soc. B 64 (1951), 747.
[47] N.J. Petch, The cleavage strength of polycrystals, J Iron Steel Inst 174 (1953) 25–28.
[48] M. Fellah, L. Aissani, M. Abdul Samad, A. Purnama, H. Djebaili, A. Montagne, A. Iost, C. Nouveau, Effect of Zr content on friction and wear behavior of Cr-Zr-N coating system, Int. J. Appl. Ceram. Technol. 15 (3) (2018) 701–715.
[49] J.G. Han, H.S. Myung, H.M. Lee, L.R. Shaginyan, Microstructure and mechanical properties of Ti-Ag-N and Ti-Cr-N superhard nanostructured coatings, Surf. Coating. Technol. 174–175 (2003) 738–743.
[50] S.J. Bull, Failure modes in scratch adhesion testing, Surf. Coating. Technol. 50 (1) (1991) 25–32.
[51] M. Larsson, M. Olsson, P. Hedenqvist, S. Hogmark, Mechanisms of coating failure as demonstrated by scratch and indentation testing of TiN coated HSS, Surf. Eng. 16 (5) (2000) 436–444.

[52] S. Zhang, X. Zhang, Toughness evaluation of hard coatings and thin films, Thin Solid Films 520 (7) (2012) 2375–2389.
[53] K. Holmberg, A. Laukkanen, H. Ronkainen, K. Wallin, S. Varjus, J. Koskinen, Tribological contact analysis of a rigid ball sliding on a hard coated surface: Part I: modelling stresses and strains, Surf. Coating. Technol. 200 (12–13) (2006) 3793–3809.
[54] L. Kaufman, E.V. Clougherty, Investigation of Boride Compounds for Very High Temperature Applications, RTD-TRD-N63-4096, Part II, ManLabs Inc., Cambridge, MA, 1965.
[55] I.C.I. Okafor, R.G. Reddy, The oxidation behavior of high-temperature aluminides, JOM 51 (6) (1999) 35–40.
[56] B. Bakhit, A. Akbari, F. Nasirpouri, M.G. Hosseini, Corrosion resistance of Ni-Co alloy and Ni-Co/SiC nanocomposite coatings electrodeposited by sediment codeposition technique, Appl. Surf. Sci. 307 (2014) 351–359.
[57] ASM Handbook, Corrosion: Fundamentals, Testing, and Protection, ASM International, Materials Park Ohio, 2003.
[58] B. Bakhit, A. Akbari, Nanocrystalline Ni-Co alloy coatings: electrodeposition using horizontal electrodes and corrosion resistance, J. Coating Technol. Res. 10 (2) (2013) 285–295.
[59] J.W. Dini, The Materials Science of Coatings and Substrates, William Andrew publishing, Noyes, 1993.
[60] B. Bakhit, A. Akbari, Effect of particle size and co-deposition technique on hardness and corrosion properties of Ni-Co/SiC composite coatings, Surf. Coating. Technol. 206 (23) (2012) 4964–4975.
[61] T. Rabizadeh, S.R. Allahkaram, Corrosion resistance enhancement of Ni-P electroless coatings by incorporation of nano-SiO_2 particles, Mater. Des. 32 (1) (2011) 133–138.